ACS OMEGA

Open Access

http://pubs.acs.org/journal/acsodf

Article

Rational Construction of MOF-Derived Porous $ZnTiO_3/TiO_2$ Heterostructured Photocatalysts with Remarkable Photocatalytic Performance

Fayun Wei, Yiwen Huang, Guangyu Zhang, Jiamu Dai, Ruiqing Li, Haifeng Zhang, Mingzheng Ge,* and Wei Zhang*

Cite This: *ACS Omega* 2023, 8, 41765−41772

Read Online

ACCESS | Metrics & More | Article Recommendations | Supporting Information

ABSTRACT: TiO_2 has been widely used in photodegradation of pollutants, but it suffers from inferior photocatalytic performance under solar light illumination. Thus, novel porous $ZnTiO_3/TiO_2$ heterostructured photocatalysts are constructed by hydrothermal and carbonization techniques using ZIF-8 as a sacrificial template. After coating with TiO_2, ZIF-8 nanocubes are selectively etched and subsequently coprecipitated with Ti ions during the hydrothermal process. Thereafter, the pores generated from carbonized ZIF-8 provide a large specific surface area and abundant active reaction sites for photocatalysis after annealing, producing stable $ZnTiO_3/TiO_2$ nanocomposites. Thus, porous $ZnTiO_3/TiO_2$ heterostructured photocatalysts exhibit excellent photocatalytic performance under solar light irradiation due to the boosted electron−hole separation/transfer. The kinetic constant of $ZnTiO_3/TiO_2$ nanocomposites (4.66×10^{-1} min^{-1}) is almost 100 and 3.7 times higher than that of self-degradation (4.69×10^{-3} min^{-1}) and TiO_2 (1.27×10^{-1} min^{-1}), respectively. This facile strategy provides a deep insight into synthesizing heterostructured photocatalysts with high efficiency in the field of environmental remediation.

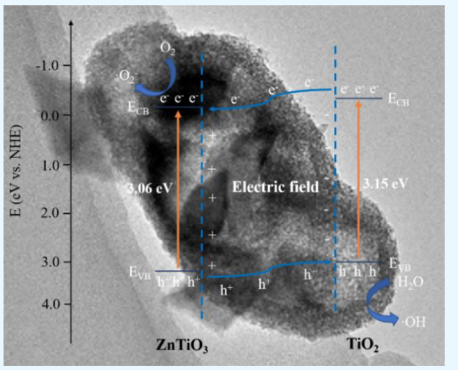

1. INTRODUCTION

Environmental problems, especially water pollution, have threatened the health of humans and organisms. Recently, semiconductor photocatalysis technology exhibits potential prospects in solving these environmental pollution problems.[1−4] Titanium dioxide (TiO_2), discovered by Fujishima and Honda in 1972 for water splitting,[5] has been attracted numerous interests and considered as one of the most promising photocatalysts candidates for organic pollutants degradation when compared to other semiconductors due to the strong oxidation property, long-term photostability, environmental friendliness, and low cost.[6−8] However, the photocatalytic activity of TiO_2 is limited by two main inherent shortcomings. The band gap of TiO_2 is wide (anatase: 3.2 eV, rutile: 3.0 eV); meanwhile, its spectral response range is very narrow. Therefore, photocatalysis can be activated only under UV light irradiation, exhibiting low photocatalytic activity under visible light illumination.[9−12] Besides, the recombination of photogenerated electron/hole pairs leads to low quantum efficiency, which greatly decreases its photocatalytic performance.[13−15]

In order to overcome these challenges, doping with metal/nonmetal elements, or compositing TiO_2 with metal, nonmetal, and other semiconductors are effective ways to improve the photocatalytic activity.[16−19] Constructing heterojunctions is regarded as an effective way to improve the utilization efficiency of solar light and suppress the recombination of electrons/hole pairs by building an internal electric field at the heterojunction interface.[20−22] The perovskite-typed materials (ABO_3) have become much more popular due to their superior photocatalytic activity under both UV and visible light irradiation.[23−25] Their structure is very stable and flexible by varying the composition of A and B sites to optimize the electronic and catalytic properties.[26−28] Among them, zinc titanate ($ZnTiO_3$) is one of the most promising photocatalysts to be applied in the degradation of pollutants and water splitting, which is considered as an ideal candidate to couple with TiO_2 for improving the photocatalytic performance of TiO_2 via creation of heterojunctions.

From a materials perspective, metal−organic frameworks (MOFs), consisting of metal ions and organic poly complex linkers, have been widely used in gas adsorption/separation, water remediation, drug delivery, energy storage, and conversion because of the large specific surface area, tunable

Received: August 24, 2023
Revised: October 10, 2023
Accepted: October 11, 2023
Published: October 27, 2023

functionalities, homogeneous pore size, and chemical stability.[29−31] Meanwhile, MOFs have been demonstrated that they can act as precursors or template materials for the fabrication of other desirable novel nanomaterials and porous nanostructured materials.[32−34] For example, Co-based nanoparticles encapsulated in a hollow N-doped carbon matrix were developed by pyrolysis and an oxidation strategy by using ZIF-67 as a precursor. Benefiting from the synergetic effects of its abundant oxygen vacancies, nitrogen-doped carbon as well as the efficient mass transfer of hollow structures, the optimal samples exhibited high activity toward oxygen reduction and evolution reactions.[35] Besides, the Z-scheme Co_9S_8/CdS heterostructure was fabricated by sulfidation of the ZIF-67 precursor. These MOF-derived heterostructured composites delivered a high photocatalytic H_2 evolution efficiency of 10,321 μmol g^{-1} h^{-1} and 99.9% selectivity to benzyl-alcohol oxidation.[36] Overall, MOF-derived nanoporous catalysts have been successfully constructed and applied in various fields ranging from environmental remediation to energy storage and conversion.[37−40] Therefore, we hypothesize that rational construction of $ZnTiO_3/TiO_2$ heterostructures via using ZIF-8 as a template can further improve the photocatalytic activity under solar light due to the improved separation and transfer of photogenerated carriers, along with low recombination rate.

Herein, we have developed a facile synthetic strategy to construct porous $ZnTiO_3/TiO_2$ composited photocatalysts with heterojunctions via a combination method of precipitation, hydrothermal, and carbonization technique using ZIF-8 as a sacrificial template. Core−shell ZIF-8@TiO_2 composites were fabricated via a precipitation method. After the hydrothermal process, ZIF-8 nanocubes were selectively etched and replaced by Ti ions. Subsequently, porous $ZnTiO_3/TiO_2$ composited photocatalysts with large specific surface area and abundant active reaction sites were achieved after heat treatment. Thus, porous $ZnTiO_3/TiO_2$ composited photocatalysts displayed superior photocatalytic performance due to the suppressed recombination of electron/hole pairs and widened visible light adsorption range via formation of heterojunctions. Obviously, the kinetic constant of $ZnTiO_3/TiO_2$ nanocomposites (4.66×10^{-1} min^{-1}) is almost 100 and 3.7 times higher than that of self-degradation (4.69×10^{-3} min^{-1}) and TiO_2 (1.27×10^{-1} min^{-1}), respectively. This facile strategy opens a new way of designing efficient heterogeneous semiconductor photocatalysts in water remediation.

2. EXPERIMENTAL SECTION

2.1. Synthesis of Core−Shell ZIF-8@TiO_2 Composites. Synthesis of zeolitic imidazolate framework-8 (ZIF-8): 1.4848 g of 2-methylimidazole and 9 mg of cetyltrimethylammonium bromide (CTAB) were dissolved in 10 mL of methanol to obtain solution A. Meanwhile, 0.6325 g of zinc nitrate hexahydrate was dissolved in 30 mL of methanol to obtain solution B. Then, solution A was poured into solution B with stirring at 500 rpm for 12 h. Finally, ZIF-8 was achieved by repeated washing with methanol and centrifugation three times.

Synthesis of core−shell ZIF-8@TiO_2 composites: ZIF-8 was dispersed in 100 mL of ethanol under ultrasonication for 20 min. Then, 0.3042 g of hexadecylamine and 0.65 mL of ammonia were poured into ZIF-8 solution with stirring for 10 min. Subsequently, 1.13 mL of tetraisopropyl orthotitanate was added into the above solution with stirring for 60 min. Finally, core−shell ZIF-8@TiO_2 composites were obtained via washing, centrifugation and freeze-drying. For comparison, TiO_2 was achieved by the same method without adding ZIF-8.

2.2. Synthesis of Porous $ZnTiO_3/TiO_2$ Composited Photocatalysts. 0.5 g portion of ZIF-8@TiO_2 composites was dissolved in 30 mL of deionized water, and then the mixture was put into a 50 mL stainless steel autoclave, which was kept at 180 °C for 24 h in an electrical oven. After that, the product is centrifuged with ethanol three times, which was defined as H-ZIF-8@TiO_2. Finally, porous $ZnTiO_3/TiO_2$ composites are achieved by annealing the product in an Ar atmosphere at different temperatures (350, 500, 650, and 800 °C) for 5 h. Pure ZIF-8 and TiO_2 also underwent the same hydrothermal process, which was named as H-ZIF-8 and H-TiO_2.

2.3. Characterizations. The morphology of as-prepared samples are investigated by field emission scanning electron microscopy (FESEM, ZEISS Gemini 300) and transmission electron microscopy (TEM, JEOL JEM-2100HR). An energy-dispersive X-ray (EDX) spectrometer fitted to TEM is used for elemental and structural analysis. The structure of the sample is characterized by X-ray diffractometer (XRD, Rigaku Ultima IV), and the chemical composition of the sample was analyzed by X-ray photoelectron spectroscopy (XPS, Thermo Scientific K-Alpha$^+$). With $BaSO_4$ as the reference, the UV−visible diffuse reflectance spectrum (UV−vis DRS) of the nanocomposite film was characterized by a Shimadzu UV-2600 spectrophotometer in the range of 200−800 nm.

2.4. Photocatalytic Measurements. The activity of photocatalytic degradation of MB (20 mg/L) was investigated. 0.1 g of powder was put into 30 mL of MB solution and placed in the dark for a period of time. The adsorption performance was tested every 30 min until an adsorption−desorption equilibrium was reached. Under solar light (xenon lamp, 1000 W) irradiation, the supernatant was taken at regular intervals and determined by a UV−vis DRS spectrophotometer. The focused incident light intensity was ca. 100 mW cm^{-2}. The content of residual MB was determined by universal analysis of a Shimadzu UV-2600.

3. RESULTS AND DISCUSSION

The schematic illustration for constructing $ZnTiO_3/TiO_2$ heterostructured photocatalysts is displayed in Figure 1.

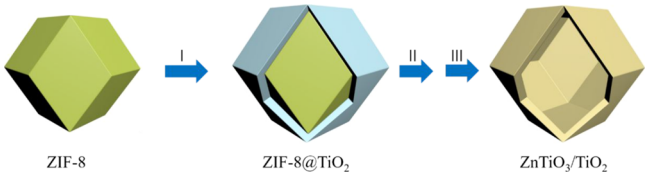

Figure 1. Schematic illustration for the fabrication process of MOF-derived porous $ZnTiO_3/TiO_2$ heterostructured photocatalysts: (I) uniform TiO_2 coating; (II) template removal by hydrothermal treatment; (III) formation of $ZnTiO_3/TiO_2$ heterostructures via annealing in an Ar atmosphere.

First, uniform polyhedra ZIF-8 nanoparticles were fabricated as templates. Second, ZIF-8 were uniformly encapsulated by TiO_2 via a kinetic-controlled deposition method, generating core−shell ZIF-8/TiO_2 nanocomposites. Third, zinc titanium composites with hollow structures were achieved via Ostwald ripening process after hydrothermal treatment, where ZIF-8 was selectively etched and subsequently coprecipitated with Ti

https://doi.org/10.1021/acsomega.3c06307
ACS Omega 2023, 8, 41765−41772

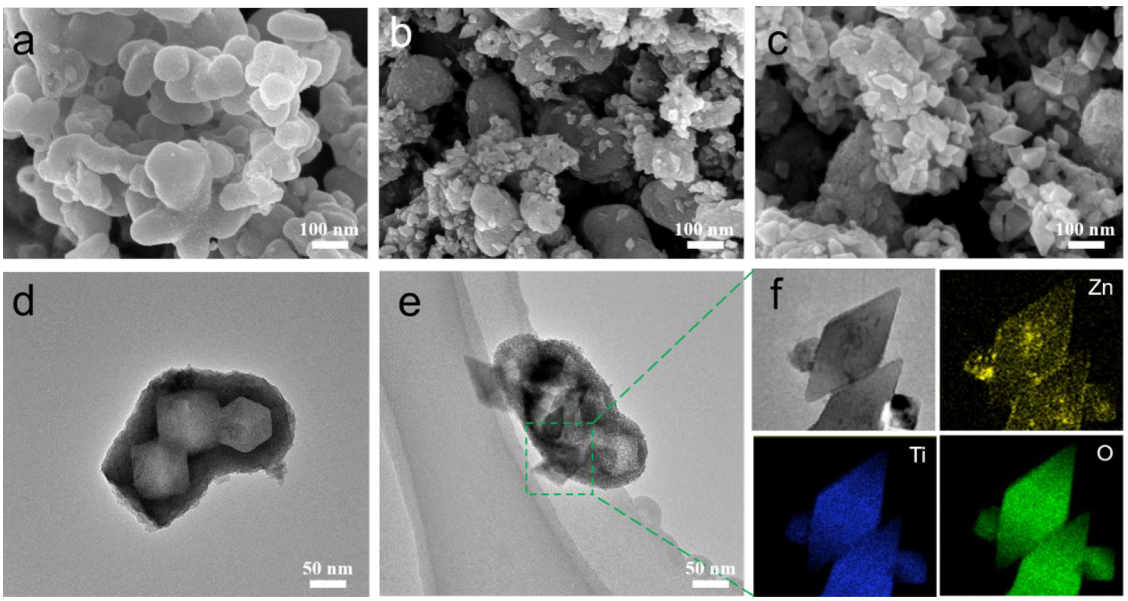

Figure 2. (a) SEM images of core−shell ZIF-8@TiO_2; (b) SEM and (d) TEM images of ZIF-8@TiO_2 after hydrothermal process. (c) SEM, (e) TEM images, and (f) EDX mapping spectra of $ZnTiO_3/TiO_2$ heterostructured composites annealed at 650 °C in an Ar atmosphere.

ions. Finally, porous $ZnTiO_3/TiO_2$ heterostructured photocatalysts were obtained via calcining in an Ar atmosphere.

Obviously, the surface of pure polyhedra of ZIF-8 was smooth. After coprecipitation reaction, ZIF-8 nanoparticles tended to aggregate to form bigger peanut-shaped particles with the size ranging from 100 to 260 nm, which were uniformly encapsulated by TiO_2 deposition layer (Figure 2a). After hydrothermal process, hollow porous zinc titanium composites were achieved, which were selectively etched and substituted by Ti ions (Figure 2b,d). Meanwhile, the surface of the composites become rough, and some nanoparticles change into octahedral shapes owing to the Ostwald ripening process. Besides, the $ZnTiO_3/TiO_2$ composited photocatalysts exhibit the similar morphology after annealing in an Ar atmosphere (Figure 2c). The hollow structure of $ZnTiO_3/TiO_2$ composites was distinctly displayed in the TEM image (Figure 2e). Furthermore, the elemental mapping images revealed that Ti, Zn and O elements were uniformly dispersed on the surface of the $ZnTiO_3/TiO_2$ composites, indicating successful synthesis of $ZnTiO_3/TiO_2$ heterostructures (Figure 2f).

In addition, SEM images of ZIF-8 and TiO_2 before and after the hydrothermal process are displayed in Figure 3. The surface of pure polyhedra ZIF-8 was smooth, and the diameter was ∼90 nm before hydrothermal treatment (Figure 3a). After hydrothermal treatment, the shape of polyhedra ZIF-8 changed into nanorods with lengths of 200−400 nm (Figure 3b). It may be attributed to that under high temperature and pressure, ZIF-8 with smaller particle size was dissolved and recrystallized to form new nanorod shapes due to the Ostwald ripening effect.[41] Meanwhile, the influence of the hydrothermal process on TiO_2 was also conducted. Before hydrothermal treatment, TiO_2 exhibited a spherical structure with a diameter of about 450−600 nm and the surface was relatively smooth (Figure 3c). While after hydrothermal treatment, the spherical structure remained unchanged, but the surface became rougher (Figure 3d). Meanwhile, it can be seen that the sphere itself was composed of extremely small TiO_2 nanoparticles with seize of ∼10 nm on its surface. In addition, the effect of annealing temperature on $ZnTiO_3/TiO_2$ heterostructured

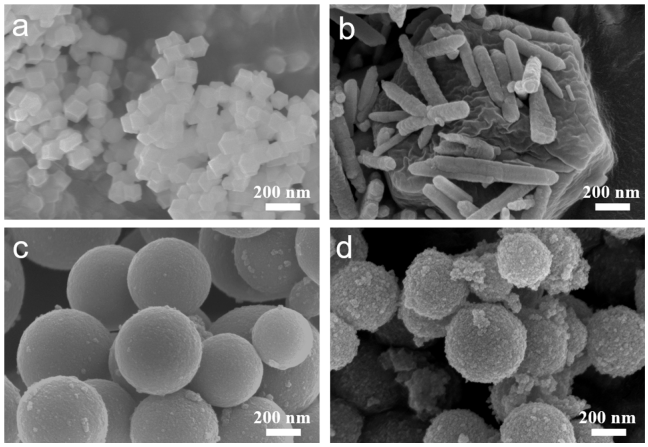

Figure 3. SEM images of (a,b) ZIF-8 and (c,d) TiO_2 before and after the hydrothermal process.

composites has also been also investigated. When increasing the annealing temperature from 350 to 650 °C, $ZnTiO_3/TiO_2$ heterostructured photocatalysts still maintained the original morphology (Figure S1a−c). However, elevating the annealing temperature to 800 °C leaded to the total collapse of the octahedral structure, decreasing the specific surface area (Figure S1d).

XRD spectra of ZIF-8, TiO_2, and core−shell ZIF-8@TiO_2 nanocomposites before and after the hydrothermal process are shown in Figure 4. The representative peaks at 10.4°, 12.7°, 14.8°, 16.4°, and 18.0° corresponded to the (002), (112), (022), (013), and (222) crystal planes of ZIF-8.[42] As for pure TiO_2, no existence of peaks for TiO_2 indicated the amorphous properties of TiO_2. Meanwhile, after TiO_2 deposition, the intensity of ZIF-8 representative peaks decreased, and there were no peaks for TiO_2, indicating successful synthesis of core−shell ZIF-8@TiO_2. While after the hydrothermal process, the new diffraction peaks at 31.8°, 34.4°, and 36.3° were related to ZnO (79-2205), indicating that ZIF-8 gradually transforms into ZnO during the hydrothermal process (Figure

https://doi.org/10.1021/acsomega.3c06307
ACS Omega 2023, 8, 41765−41772

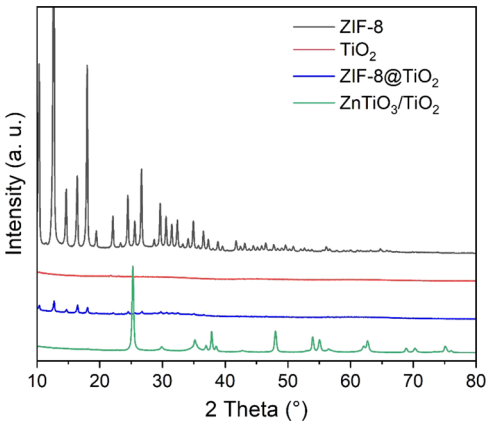

Figure 4. XRD spectrum of ZIF-8, pure TiO_2, ZIF-8@TiO_2, and $ZnTiO_3/TiO_2$ heterostructured photocatalysts.

S2). Furthermore, after calcining in Ar at 650 °C for 5 h, there appeared representative peaks for anatase TiO_2. The diffraction peaks at 25.3°, 37.8°, and 48.0° belong to the (101), (004), and (200) crystal planes of anatase TiO_2 (JCPDS 21-1272).[43,44] Meanwhile, the diffraction peak at 30.0°, 35.4,° and 56.9° corresponds to cubic $ZnTiO_3$, verifying construction of $ZnTiO_3/TiO_2$ heterojunctions.[45,46] Furthermore, the effect of the annealing temperature on the structure of $ZnTiO_3/TiO_2$ nanocomposites has been studied. It could be observed that there were only diffraction peaks of anatase TiO_2 at 350 and 500 °C (Figure S3). When increasing the annealing from 650 to 800 °C, the diffraction peaks at 14.9°, 23.6°, 26.0° and 43.0° were related to cubic $ZnTiO_3$, while the diffraction peaks at 32.8°, 40.5°, and 53.4° were related to hexagonal $ZnTiO_3$.

N_2 adsorption−desorption isotherms of core−shell ZIF-8@TiO_2 composites before and after hydrothermal process are displayed in Figure 5. The specific surface area of ZIF-8 was 1139.5 $m^2\ g^{-1}$, and the pore diameter was ∼2 nm with a large number of micropores (Figure S4), which was beneficial for adsorption. Besides, the N_2 adsorption desorption isotherm of ZIF-8@TiO_2 belonged to type IV and exhibited H_2 hysteresis in the range of 0.5−0.9 for P/P_0, indicating that ZIF-8@TiO_2 has mesoporous structure (Figure 5a).[47] ZIF-8@TiO_2 exhibited a much smaller specific surface area of 75.2 $m^2\ g^{-1}$ than ZIF-8, and the pore size distribution of is mainly at 10 nm, indicating that ZIF-8 were successfully wrapped by TiO_2 shell and exhibited the similar porous properties to ZIF-8. Similarly, ZIF-8@TiO_2 after hydrothermal process (H-ZIF-8@TiO_2) exhibited a much higher specific surface area of 219.2 $m^2\ g^{-1}$ than that of TiO_2@ZIF-8 before hydrothermal process, and the pore diameter is mainly located at 15−20 and 35−60 nm, indicating that H-ZIF-8@TiO_2 nanocomposites had mesopores and macropores (Figure 5b). The differences between TiO_2@ZIF-8 and H-ZIF-8@TiO_2 composites were attributed to the hydrothermal process, resulting in an interior hollow structure and some polyhedral particles changing into smaller octahedral particles, thus increasing the specific surface area.

Figure 6a shows the UV−vis DRS absorption spectrum of TiO_2 and $ZnTiO_3/TiO_2$ heterostructured photocatalysts. TiO_2 displayed high UV light absorption capability but exhibited low visible light absorption capability, which was due to the large band gap and fast recombination of photogenerated electron/hole pairs. Compared with TiO_2, the visible light absorption region of $ZnTiO_3/TiO_2$ nanocomposites was largely enhanced, which was attributed to the strong visible-light sensitive property of $ZnTiO_3$. The band gap of these samples can be calculated by the UV−vis DRS absorption spectrum and eq 1[48]:

$$(\alpha h\nu)^2 = A(h\nu - E_g) \quad (1)$$

where A is a constant, α is the optical absorption coefficient, h is the Planck constant, ν is the optical frequency, and E_g is the forbidden bandwidth of the material. The band gaps of TiO_2 and $ZnTiO_3/TiO_2$ heterostructured photocatalysts were calculated as 3.2 and 2.7 eV, respectively. The lowest band gap of $ZnTiO_3/TiO_2$ indicated the higher photocatalytic activity than pure TiO_2 due to the suppressed electron/holes recombination and rapid transfer of charge carriers via construction of $ZnTiO_3/TiO_2$ heterostructures (Figure 6b).

The photocatalytic performance of TiO_2 and $ZnTiO_3/TiO_2$ nanocomposites for degradation of MB under solar light irradiation is displayed in Figure 7. There were almost no concentration changes for MB without the existence of photocatalysts in the dark, and the degradation rate of MB was lower than 10% under solar light irradiation. The adsorption capacity of TiO_2 in 60 min could reach 7.5%, while the $ZnTiO_3/TiO_2$ nanocomposites could reach 39.4% due to the better wettability to pollutants and high specific surface area. After 5 min, the degradation efficiency of $ZnTiO_3/TiO_2$ nanocomposites was 91.2%, much higher than that of TiO_2 (23.2%) (Figure 7a), indicating that the

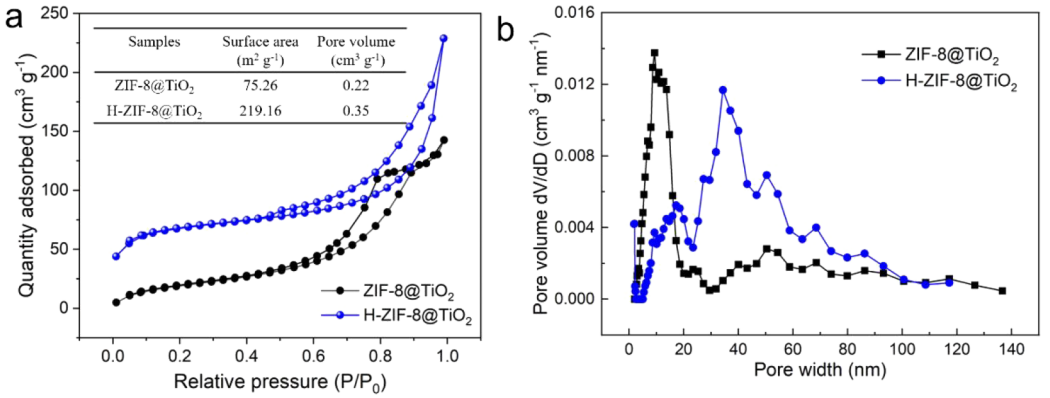

Figure 5. (a) N_2 adsorption−desorption isotherms and (b) pore size distribution of core−shell TiO_2@ZIF-8 composites before and after the hydrothermal process.

https://doi.org/10.1021/acsomega.3c06307
ACS Omega 2023, 8, 41765−41772

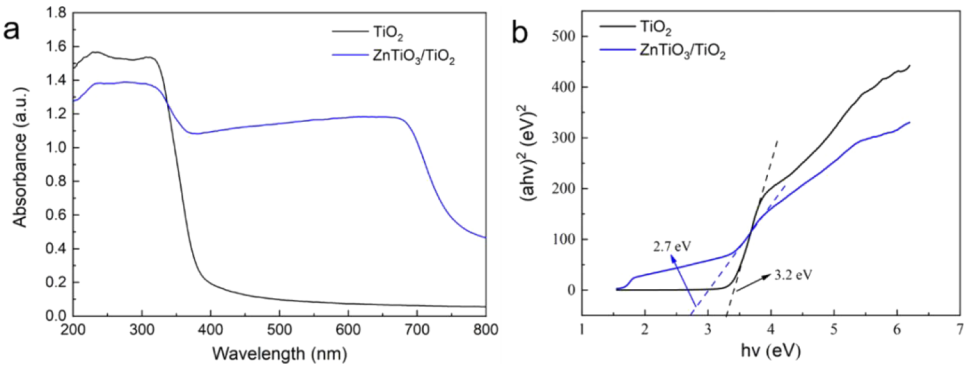

Figure 6. (a) UV−vis DRS absorption spectrum and (b) the corresponding band gap of TiO_2 and $ZnTiO_3/TiO_2$ nanocomposites, respectively.

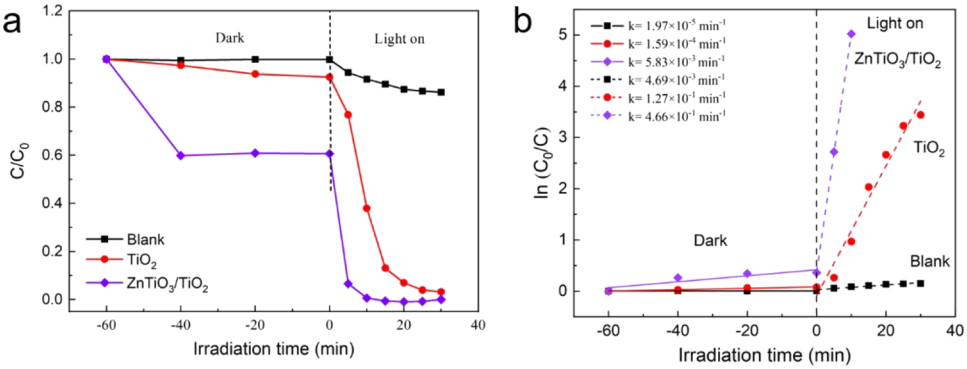

Figure 7. (a) Photodegradation efficiency and (b) kinetic curves of MB self-degradation, TiO_2, and $ZnTiO_3/TiO_2$ nanocomposites under solar light irradiation.

heterostructures improved the degradation efficiency of $ZnTiO_3/TiO_2$ photocatalysts toward MB under solar light irradiation. After 30 min, the degradation efficiency of both TiO_2 and $ZnTiO_3/TiO_2$ nanocomposites toward MB was approximately 100%. The pseudo-first-order kinetic was used to study the photocatalytic degradation activity of MB, and the formula was as follows[49]:

$$\ln(C_0/C) = Kt \quad (2)$$

where C_0, C, K, and T are the initial concentration of MB, the residual concentration of MB in the solution, the pseudo-first-order rate constant, and the illumination time t, respectively. The pseudo-first-order kinetics of TiO_2 and $ZnTiO_3/TiO_2$ nanocomposites under solar light irradiation is shown in Figure 7b. $ZnTiO_3/TiO_2$ nanocomposites had the highest photodegradation rate constant (4.66×10^{-1} min^{-1}), which was almost 100 and 3.7 times higher than that of self-degradation (4.69×10^{-3} min^{-1}) and TiO_2 (1.27×10^{-1} min^{-1}), respectively, which was attributed to the heterostructures enhanced the photocatalytic performance due to the enhanced visible light absorption capability and depressed electron/holes recombination rate under solar light irradiation. $ZnTiO_3/TiO_2$ nanocomposites exhibited almost no removal efficiency decay toward MB degradation even after 5 recycles (Figure S5). What's more, when annealed at 350 and 500 °C, the photocatalytic degradation efficiency toward MO were 11.0 and 45.9%, respectively (Figure S6). $ZnTiO_3/TiO_2$ nanocomposites annealed at 650 °C exhibited the highest degradation rate toward MO, which was attributed to the rapid electron/hole separation/transfer construction of $ZnTiO_3/TiO_2$ heterostructures. Meanwhile, when still increasing the annealing temperature to 800 °C, $ZnTiO_3/TiO_2$ nanocomposites annealed 800 °C exhibited decreased photocatalytic activity than that of $ZnTiO_3/TiO_2$ nanocomposites annealed at 650 °C, which may be due to the destroyed structures and decreased specific surface area.

The electron−hole separation/transfer process in the $ZnTiO_3/TiO_2$ nanocomposites is shown in Figure 8. In the

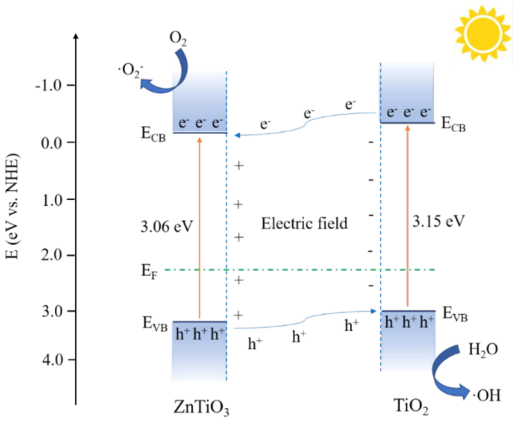

Figure 8. Proposed schematic illustration of electron−hole separation/transfer and photocatalytic degradation mechanism over $ZnTiO_3/TiO_2$ heterojunctions.

heterostructure, electrons transferred from TiO_2 to $ZnTiO_3$ because of the higher Fermi level of TiO_2. The Fermi level alignment will cause the band edges of TiO_2 and $ZnTiO_3$ to shift downward and upward, respectively, until their Fermi levels reaching equilibrium. At the equilibrium heterojunction, TiO_2 had a positive charge, while $ZnTiO_3$ had a negative

https://doi.org/10.1021/acsomega.3c06307
ACS Omega 2023, 8, 41765−41772

charge, thus, creating an opposing electric field (ξ) at the interface.[50,51] Therefore, during the process of photocatalysis, due to the influence of the electric field, the photogenerated electrons can diffuse to the conduction band of $ZnTiO_3$, and the holes can move to the valence band of TiO_2, suppressing the recombination of electrons and holes, thus enhancing the photocatalytic efficiency under solar light irradiation.

4. CONCLUSIONS

In conclusion, we have successfully constructed $ZnTiO_3/TiO_2$ heterostructured photocatalysts by hydrothermal and carbonization techniques using ZIF-8 as a sacrificial template. Heterostructured $ZnTiO_3/TiO_2$ nanocomposites exhibit excellent photocatalytic performance under solar light irradiation due to the rapid separation and transfer of photogenerated charge carriers and broadened visible light absorption region. The kinetic constants of $ZnTiO_3/TiO_2$ nanocomposites are 4.66×10^{-1} min^{-1} under solar light irradiation, which was much higher than that of self-degradation (4.69×10^{-3} min^{-1}) and TiO_2 (1.27×10^{-1} min^{-1}). Thus, this novel strategy provides a deep insight into designing advanced heterogeneous semiconductor catalysts in the field of water splitting for H_2 production, photocatalytic degradation of pollutants, etc.

■ ASSOCIATED CONTENT

Supporting Information

The Supporting Information is available free of charge at https://pubs.acs.org/doi/10.1021/acsomega.3c06307.

SEM images of $ZnTiO_3/TiO_2$ heterostructured photocatalysts annealed at different temperatures: 350, 500, 650, and 800 °C; XRD spectrum of ZIF-8, pure TiO_2, and TiO_2@ZIF-8 after the hydrothermal process; XRD spectra of $ZnTiO_3/TiO_2$ heterostructured photocatalysts annealed at different temperatures: 350, 500, 650, and 800 °C; N_2 adsorption−desorption isotherms and pore size distribution of ZIF-8; removal rate of $ZnTiO_3/TiO_2$ nanocomposites after 5 min irradiation with 5 repeated cycles; and photodegradation efficiency of $ZnTiO_3/TiO_2$ heterostructured photocatalysts annealed at different temperatures: 350, 500, 650, and 800 °C toward methyl orange (PDF)

■ AUTHOR INFORMATION

Corresponding Authors

Mingzheng Ge − *School of Textile and Clothing, Nantong University, Nantong 226019, P. R. China; Key Laboratory of Jiangsu Province for Silk Engineering, Soochow University, Suzhou 215123, P. R. China; Institute of Applied Physics and Materials Engineering, University of Macau, Macau 999078, P. R. China;* orcid.org/0000-0002-3448-116X; Email: mzge1990@ntu.edu.cn

Wei Zhang − *School of Textile and Clothing, Nantong University, Nantong 226019, P. R. China;* Email: zhangwei@ntu.edu.cn

Authors

Fayun Wei − *School of Textile and Clothing, Nantong University, Nantong 226019, P. R. China; College of Textile Science and Engineering, Zhejiang Sci-Tech University, Hangzhou 310018, P. R. China*

Yiwen Huang − *School of Textile and Clothing, Nantong University, Nantong 226019, P. R. China*

Guangyu Zhang − *School of Textile and Clothing, Nantong University, Nantong 226019, P. R. China;* orcid.org/0000-0002-1364-3350

Jiamu Dai − *School of Textile and Clothing, Nantong University, Nantong 226019, P. R. China*

Ruiqing Li − *School of Textile and Clothing, Nantong University, Nantong 226019, P. R. China*

Haifeng Zhang − *School of Textile and Clothing, Nantong University, Nantong 226019, P. R. China*

Complete contact information is available at: https://pubs.acs.org/10.1021/acsomega.3c06307

Author Contributions

F.W., Y.H., and G.Z. conceived the project and designed the experiments. R.L. and H.Z. fabricated the samples, conducted the characterizations, and performed the supercapacitor tests. M.G. and W. Z. revised the manuscript. All authors analyzed the data and contributed to the discussions.

Notes

The authors declare no competing financial interest.

■ ACKNOWLEDGMENTS

This work was supported by the National Natural Science Foundation of China (52202256), the Natural Science Foundation of Jiangsu Province of China (BK20220612), the Natural Science Foundation of Nantong City of China (JC22022024, MS12021006), the Science and Technology Development Fund, and the Opening Project of Key Laboratory of Jiangsu Province for Silk Engineering, Soochow University (KJS2277). We also acknowledge the funds from Jiangsu University "Qinglan Project". We thank Nantong University Analysis and Testing Center for the technical support.

■ REFERENCES

(1) Lee, B. H.; Park, S.; Kim, M.; Sinha, A. K.; Lee, S. C.; Jung, E.; Chang, W. J.; Lee, K. S.; Kim, J. H.; Cho, S. P.; Kim, H.; Nam, K. T.; Hyeon, T. Reversible and cooperative photoactivation of single-atom Cu/TiO_2 photocatalysts. *Nat. Mater.* **2019**, *18*, 620−626.

(2) Zhang, W. Q.; Fu, C. F.; Low, J. X.; Duan, D. L.; Ma, J.; Jiang, W. B.; Chen, Y. H.; Liu, H. J.; Qi, Z. M.; Long, R.; Yao, Y. F.; Li, X. B.; Zhang, H.; Liu, Z.; Yang, J. L.; Zou, Z. G.; Xiong, Y. J. High-performance photocatalytic nonoxidative conversion of methane to ethane and hydrogen by heteroatoms-engineered TiO_2. *Nat. Commun.* **2022**, *13*, 2806.

(3) Zhao, D. M.; Wang, Y. Q.; Dong, C. L.; Huang, Y. C.; Chen, J.; Xue, F.; Shen, S. H.; Guo, L. J. Boron-doped nitrogen-deficient carbon nitride-based Z-scheme heterostructures for photocatalytic overall water splitting. *Nat. Energy* **2021**, *6*, 388−397.

(4) Liang, F. D.; Dong, H. L.; Ji, Z. Y.; Zhang, W.; Zhang, H. F.; Cao, C. Y.; Li, H.; Liu, H. C.; Zhang, K. Q.; Lai, Y. K.; Tang, Y. X.; Ge, M. Z. Temperature-dependent synthesis of SnO_2 or Sn embedded in hollow porous carbon nanofibers toward customized lithium-ion batteries. *Sci. China Mater.* **2023**, *66*, 1736−1746.

(5) Ge, M. Z.; Cao, C. Y.; Huang, J. Y.; Li, S. H.; Chen, Z.; Zhang, K. Q.; Al-Deyab, S. S.; Lai, Y. K. A review of one-dimensional TiO_2 nanostructured materials for environmental and energy applications. *J. Mater. Chem. A* **2016**, *4*, 6772−6801.

(6) He, B. W.; Wang, Z. L.; Xiao, P.; Chen, T.; Yu, J. G.; Zhang, L. Y. Cooperative coupling of H_2O_2 production and organic synthesis over a floatable polystyrene-sphere-supported TiO_2/Bi_2O_3 S-scheme photocatalyst. *Adv. Mater.* **2022**, *34*, No. 2203225.

(7) Wang, X.; Zeng, W.; Hong, L.; Xu, W.; Yang, H.; Wang, F.; Duan, H.; Tang, M.; Jiang, H. Stress-driven lithium dendrite growth

https://doi.org/10.1021/acsomega.3c06307
ACS Omega 2023, 8, 41765−41772

mechanism and dendrite mitigation by electroplating on soft substrates. *Nat. Energy* **2018**, *3*, 227−235.
(8) Lam, E.; Reisner, E. A TiO_2-Co(terpyridine)$_2$ photocatalyst for the selective oxidation of cellulose to formate coupled to the reduction of CO_2 to syngas. *Angew. Chem., Int. Ed.* **2021**, *60*, 23306−23312.
(9) Ma, K.; Yehezkeli, O.; Domaille, D. W.; Funke, H. H.; Cha, J. N. Enhanced hydrogen production from DNA-assembled Z-Scheme TiO_2-CdS photocatalyst systems. *Angew. Chem., Int. Ed.* **2015**, *54*, 11490−11494.
(10) Song, X. Y.; Li, W. Q.; He, D.; Wu, H. Y.; Ke, Z. J.; Jiang, C. Z.; Wang, G. M.; Xiao, X. H. The "Midas Touch" transformation of TiO_2 nanowire arrays during visible light photoelectrochemical performance by carbon/nitrogen coimplantation. *Adv. Energy Mater.* **2018**, *8*, No. 800165.
(11) Wu, T. T.; Niu, P.; Yang, Y. Q.; Yin, L. C.; Tan, J.; Zhu, H. Z.; Irvin, J. T. S.; Wang, L. Z.; Liu, G.; Cheng, H. M. Homogeneous doping of substitutional nitrogen/carbon in TiO_2 plates for visible light photocatalytic water oxidation. *Adv. Funct. Mater.* **2019**, *29*, No. 1901943.
(12) Zhou, X.; Hwang, I.; Tomanec, O.; Fehn, D.; Mazare, A.; Zboril, R.; Meyer, K.; Schmuki, P. Advanced photocatalysts: pinning single atom co-catalysts on titania nanotubes. *Adv. Funct. Mater.* **2021**, *31*, No. 2102843.
(13) Liu, Y. P.; Li, Y. H.; Li, X. Y.; Zhang, Q.; Yu, H.; Peng, X. W.; Peng, F. Regulating electron-hole separation to promote photocatalytic H_2 evolution activity of nanoconfined Ru/MXene/TiO_2 catalysts. *ACS Nano* **2020**, *14*, 14181−14189.
(14) Yu, X.; Jin, X.; Chen, X. Y.; Wang, A. Z.; Zhang, J. M.; Zhang, J.; Zhao, Z. H.; Gao, M. M.; Razzari, L.; Liu, H. A microorganism bred TiO_2/Au/TiO_2 heterostructure for whispering gallery mode resonance assisted plasmonic photocatalysis. *ACS Nano* **2020**, *14*, 13876−13885.
(15) Shirai, K.; Sugimoto, T.; Watanabe, K.; Haruta, M.; Kurata, H.; Matsumoto, Y. Effect of water adsorption on carrier trapping dynamics at the surface of anatase TiO_2 nanoparticles. *Nano Lett.* **2016**, *16*, 1323−1327.
(16) Dalanta, F.; Kusworo, T. D.; Aryanti, N. Synthesis, characterization, and performance evaluation of UV light-driven Co-TiO_2@SiO_2 based photocatalytic nanohybrid polysulfone membrane for effective treatment of petroleum refinery wastewater. *Appl. Catal., B* **2022**, *316*, No. 121576.
(17) Jayachitra, S.; Mahendiran, D.; Ravi, P.; Murugan, P.; Sathish, M. Highly conductive $NiSe_2$ nanoparticle as a co-catalyst over TiO_2 for enhanced photocatalytic hydrogen production. *Appl. Catal., B* **2022**, *307*, No. 121159.
(18) Yang, Y.; Zhu, B. C.; Wang, L. B.; Cheng, B.; Zhang, L. Y.; Yu, J. G. In-situ grown N, S co-doped graphene on TiO_2 fiber for artificial photosynthesis of H_2O_2 and mechanism study. *Appl. Catal., B* **2022**, *317*, No. 121788.
(19) Liu, B. S.; Wu, H.; Parkin, I. P. New insights into the fundamental principle of semiconductor photocatalysis. *ACS Omega* **2020**, *5*, 14847−14856.
(20) Almazroai, L.; El-Mekawy, R. E.; Musa, R.; Ali, L. Photocatalytic hydrogen evolution over cyanine-sensitized Ag/TiO_2. *RSC Adv.* **2022**, *12*, 15992−16002.
(21) Zhang, B.; Li, X. M.; Ma, Y. S.; Jiang, T. Y.; Zhu, Y. Y.; Ren, H. X. Visible-light photoelectrocatalysis/H_2O_2 synergistic degradation of organic pollutants by a magnetic Fe_3O_4@SiO_2@mesoporous TiO_2 catalyst-loaded photoelectrode. *RSC Adv.* **2022**, *12*, 30577−30587.
(22) Zhang, Y. Q.; Xu, N.; Liu, Y.; Zhang, X. S.; Li, W. Z.; Zhao, H. T.; Luan, J. Synthesis of a 2D Cu@TiO_2 composite via the design of a 1D Cu-based coordination polymer precursor for efficient and selective photodegradation of dyes. *RSC Adv.* **2022**, *12*, 9363−9372.
(23) Peng, J. R.; Wang, Y.; Bai, J. Y.; Ma, D. X.; Zhao, R. Y.; Han, J. S.; Wang, L. High-efficiency hollow $Zn_{0.98}Cu_{0.02}Se$/ZnS/$ZnTiO_3$ photocatalyst for hydrogen production application. *Fuel* **2022**, *325*, No. 124937.
(24) Lin, B. Y.; Li, S. S.; Peng, Y. N.; Chen, Z. H.; Wang, X. MOF-derived core/shell C-TiO_2/$CoTiO_3$ type II heterojunction for efficient photocatalytic removal of antibiotics. *J. Hazard. Mater.* **2021**, *406*, No. 124675.
(25) Li, X. B.; Xiong, J.; Huang, J. T.; Feng, Z. J.; Luo, J. M. Novel g-C_3N_4/h 'ZnTiO_3-a' TiO_2 direct Z-scheme heterojunction with significantly enhanced visible-light photocatalytic activity. *J. Alloys Compd.* **2019**, *774*, 768−778.
(26) Tijare, S. N.; Joshi, M. V.; Padole, P. S.; Mangrulkar, P. A.; Rayalu, S. S.; Labhsetwar, N. K. Photocatalytic hydrogen generation through water splitting on nano-crystalline $LaFeO_3$ perovskite. *Int. J. Hydrogen Energy* **2012**, *37*, 10451−10456.
(27) Wei, H. M.; Yang, C.; Wu, Y. Q.; Cao, B. Q.; Lorenz, M.; Grundmann, M. From energy harvesting to topologically insulating behavior: ABO_3-type epitaxial thin films and superlattices. *J. Mater. Chem. C* **2020**, *8*, 15575−15596.
(28) Purohit, S.; Yadav, K. L.; Satapathi, S. Bandgap Engineering in a staggered-type oxide perovskite heterojunction for efficient visible light-driven photocatalytic dye degradation. *Langmuir* **2021**, *37*, 3467−3476.
(29) Alshorifi, F. T.; El Dafrawy, S. M.; Ahmed, A. I. Fe/Co-MOF nanocatalysts: greener chemistry approach for the removal of toxic metals and catalytic applications. *ACS Omega* **2022**, *7*, 23421−23444.
(30) Alzard, R. H.; Siddig, L. A.; Abdelhamid, A. S.; Alzamly, A. Visible-light-driven photocatalytic coupling of neat benzylamine over a bi-ellagate metal-organic framework. *ACS Omega* **2022**, *7*, 36689−36696.
(31) Nayak, A.; Viegas, S.; Dasari, H.; Sundarabal, N. Cu-BDC and Cu_2O derived from Cu-BDC for the removal and oxidation of asphaltenes: a comparative study. *ACS Omega* **2022**, *7*, 34966−34973.
(32) Cai, Z. Z.; Liu, Q.; Li, H. X.; Wang, J. Y.; Tai, G. Y.; Wang, F.; Han, J. G.; Zhu, Y. L.; Wu, G. Y. Waste-to-resource strategy to fabricate functionalized MOFs composite material based on durian shell biomass carbon fiber and Fe_3O_4 for highly efficient and recyclable dye adsorption. *Int. J. Mol. Sci.* **2022**, *23*, 5900.
(33) Hamedi, A.; Trotta, F.; Borhani Zarandi, M.; Zanetti, M.; Caldera, F.; Anceschi, A.; Nateghi, M. R. In situ synthesis of MIL-100(Fe) at the surface of Fe_3O_4@AC as highly efficient dye adsorbing nanocomposite. *Int. J. Mol. Sci.* **2019**, *20*, 5612.
(34) Saura-Sanmartin, A. Photoresponsive metal-organic frameworks as adjustable scaffolds in reticular chemistry. *Int. J. Mol. Sci.* **2022**, *23*, 7121.
(35) Ding, D. N.; Shen, K.; Chen, X. D.; Chen, H. R.; Chen, J. Y.; Fan, T.; Wu, R. F.; Li, Y. W. Multi-level architecture optimization of MOF-templated Co-based nanoparticles embedded in hollow n-doped carbon polyhedra for efficient OER and ORR. *ACS Catal.* **2018**, *8*, 7879−7888.
(36) Liu, M.; Qiao, L. Z.; Dong, B. B.; Guo, S.; Yao, S.; Li, C.; Zhang, Z. M.; Lu, T. B. Photocatalytic coproduction of H_2 and industrial chemical over MOF-derived direct Z-scheme heterostructure. *Appl. Catal., B* **2020**, *273*, No. 119066.
(37) Song, Y. T.; Peng, Y. W.; Yao, S.; Zhang, P.; Wang, Y. J.; Gu, J. M.; Lu, T. B.; Zhang, Z. M. Co-POM@MOF-derivatives with trace cobalt content for highly efficient oxygen reduction. *Chin. Chem. Lett.* **2022**, *32*, 1047.
(38) Zhong, L. X.; Mao, B. D.; Liu, M.; Liu, M. Y.; Sun, Y. Q.; Song, Y. T.; Zhang, Z. M.; Lu, T. B. Construction of hierarchical photocatalysts by growing $ZnIn_2S_4$ nanosheets on Prussian blue analogue-derived bimetallic sulfides for solar co-production of H_2 and organic chemicals. *J. Energy Chem.* **2021**, *54*, 386.
(39) Zhang, Y. P.; Xua, J. X.; Zhou, J.; Wang, L. Metal-organic framework-derived multifunctional photocatalysts. *Chin. J. Catal.* **2022**, *43*, 971.
(40) Wang, L.; Gong, N.; Zhou, Z.; Zhang, Q. C.; Peng, W. C.; Li, Y.; Zhang, F. B.; Fan, X. B. A MOF derived hierarchically porous 3D N-CoP_x/Ni_2P electrode for accelerating hydrogen evolution at high current densities. *Chin. J. Catal.* **2022**, *43*, 1176.
(41) Tian, H.; Wang, S. C.; Zhang, C.; Veder, J. P.; Pan, J.; Jaroniec, M.; Wang, L. Z.; Liu, J. Design and synthesis of porous $ZnTiO_3$/TiO_2

https://doi.org/10.1021/acsomega.3c06307
ACS Omega 2023, 8, 41765−41772

nanocages with heterojunctions for enhanced photocatalytic H_2 production. *J. Mater. Chem. A* **2017**, *5*, 11615−11622.
(42) Sun, W. Z.; Zhai, X. S.; Zhao, L. Synthesis of ZIF-8 and ZIF-67 nanocrystals with well-controllable size distribution through reverse microemulsions. *Chem. Eng. J.* **2016**, *289*, 59−64.
(43) Ge, M. Z.; Li, Q. S.; Cao, C. Y.; Huang, J. Y.; Li, S. H.; Zhang, S. N.; Chen, Z.; Zhang, K. Q.; Al-Deyab, S. S.; Lai, Y. K. One-dimensional TiO_2 nanotube photocatalysts for solar water splitting. *Adv. Sci.* **2017**, *4*, No. 1600152.
(44) Yu, J. D.; Xiang, S. W.; Ge, M. Z.; Zhang, Z. Y.; Huang, J. Y.; Tang, Y. X.; Sun, L.; Lin, C. J.; Lai, Y. K. Rational construction of $LaFeO_3$ perovskite nanoparticle-modified TiO_2 nanotube arrays for visible-light driven photocatalytic activity. *Coatings* **2018**, *8*, 374.
(45) Jaramillo-Fierro, X.; Cuenca, G.; Ramon, J. The effect of La^{3+} on the methylene blue dye removal capacity of the $La/ZnTiO_3$ photocatalyst, a DFT Study. *Nanomaterials* **2022**, *12*, 3137.
(46) Seo, H. J.; Yu, J. H.; Ananth, A.; Jeong, R. H.; Boo, J. H. Synthesis of zinc-titanium oxide nanocomposites by plasma jet and its application to photocatalyst. *Catalysts* **2022**, *12*, 1020.
(47) Ru, Z. W.; Zhang, X.; Zhang, M.; Mi, J.; Cao, C. Y.; Yan, Z. F.; Ge, M. Z.; Liu, H. C.; Wang, J. C.; Zhang, W.; Cai, W. L.; Lai, Y. K.; Feng, Y. Bimetallic-MOF-derived $Zn_xCo_{3-x}O_4$/carbon nanofiber composited sorbents for high-temperature coal gas desulfurization. *Environ. Sci. Technol.* **2022**, *56*, 17288−17297.
(48) Zang, C. F.; Han, X. Y.; Chen, H.; Zhang, H. F.; Lei, Y. G.; Liu, H. C.; Wang, C. X.; Zhang, G. Y.; Ge, M. Z. In situ growth of ZnO/Ag_2O heterostructures on PVDF nanofibers as efficient visible-light-driven photocatalysts. *Ceram. Int.* **2022**, *48*, 27379−27387.
(49) Ge, M. Z.; Li, S. H.; Huang, J. Y.; Zhang, K. Q.; Al-Deyab, S. S.; Lai, Y. K. TiO_2 nanotube arrays loaded with reduced graphene oxide films: facile hybridization and promising photocatalytic application. *J. Mater. Chem. A* **2015**, *3*, 3491−3499.
(50) Cao, Q.; Li, Q. Q.; Pi, Z. C.; Zhang, J.; Sun, L. W.; Xu, J. Z.; Cao, Y. Y.; Cheng, J. Y.; Bian, Y. Metal-organic-framework-derived ball-flower-like porous Co_3O_4/Fe_2O_3 heterostructure with enhanced visible-light-driven photocatalytic activity. *Nanomaterials* **2022**, *12*, 904.
(51) Li, Z.; Li, R. G.; Jing, H. J.; Xiao, J. P.; Xie, H. C.; Hong, F.; Ta, N.; Zhang, X. W.; Zhu, J.; Li, C. Blocking the reverse reactions of overall water splitting on a Rh/GaN-ZnO photocatalyst modified with Al_2O_3. *Nat. Catal.* **2023**, *6*, 80−88.

https://doi.org/10.1021/acsomega.3c06307
ACS Omega 2023, 8, 41765−41772